## PHYSICS

# Synchrotron x-ray imaging visualization study of capillary-induced flow and critical heat flux on surfaces with engineered micropillars

Dong In Yu,[1]* Ho Jae Kwak,[2]* Hyunwoo Noh,[2] Hyun Sun Park,[3] Kamel Fezzaa,[4] Moo Hwan Kim[2,3]†

Over the last several decades, phenomena related to critical heat flux (CHF) on structured surfaces have received a large amount of attention from the research community. The purpose of such research has been to enhance the safety and efficiency of a variety of thermal systems. A number of theories have been put forward to explain the key CHF enhancement mechanisms on structured surfaces. However, these theories have not been confirmed experimentally because of limitations in the available visualization techniques and the complexity of the phenomena. To overcome these limitations and elucidate the CHF enhancement mechanism on the structured surfaces, we introduce synchrotron x-ray imaging with high spatial (~2 μm) and temporal (~20,000 Hz) resolutions. This technique has enabled us to confirm that capillary-induced flow is the key CHF enhancement mechanism on structured surfaces.

## INTRODUCTION

Nucleate boiling is characterized by bubble growth and collapse on heated surfaces. This boiling phenomenon is induced by differences between the temperatures of the heated surface and the liquid. Given the latent heat of nucleate bubbles, the heat transfer mechanism associated with pool boiling exhibits high-level thermal efficiency. This substantially improves the heat transfer performance. Therefore, nucleate boiling is used as the primary heat transfer mechanism in a range of research and industrial applications, such as power generation, desalination, chemical processing, refrigeration, thermal management of electronics, etc. However, when the heat flux on a heated surface gradually increases and then reaches its critical value, the surface becomes coated by a vapor film. This results in the liquid being replaced by the vapor adjacent to the heated surface. Subsequently, the efficiency of the heat transfer decreases suddenly and the heated surface burns out. This phenomenon is an inherent limitation of the nucleate boiling heat transfer mechanism. The critical heat flux (CHF) is one of the key design parameters to consider when designing safe nucleate boiling apparatuses.

For this reason, many researchers have investigated the CHF triggering mechanism. Kutateladze (1) and Zuber (2) analyzed CHF with hydrodynamic instability from a physical perspective. Haramura and Katto (3) postulated that CHF is triggered when the liquid film within the microlayer completely evaporates as a massive bubble hovers over it. Theofanous et al. (4) and Unal et al. (5) focused on the behavior of the liquid-vapor interface of the heated surface. According to their model, because the CHF phenomena are controlled by the relationship between the liquid and vapor phase, mediated via the interface, CHF is triggered when a hot spot develops irreversibly on the heated surface. In each of these studies, the CHF triggering mechanism has been found to significantly depend on the behavior and shape of the liquid-vapor interface underneath the bubbles. Therefore, to obtain experimental insights and

better understand the CHF phenomenon, we need to be able to visualize the region underneath the bubbles.

In addition, many researchers have noted CHF enhancement mechanisms. In particular, surface conditions have been varied to enhance CHF. Surface wetting characteristics, such as chemical composition and geometrical morphology, influence the behavior and shape of the liquid-vapor interface. Kandlikar (6) has postulated that CHF decreases as the contact angle increases and proposed a model of CHF based on the chemical composition of the surface. The addition of surface structures has been shown to enhance CHF beyond that predicted by classical CHF models (7–26). A number of papers have reported that the CHF increases on micro (7–14), nano (15–26), and micro/nano hierarchically structured surfaces (27–32). Many mechanisms have been proposed to explain CHF enhancement on structured surfaces. These include the effects of vapor recoil and solid-liquid surface adhesion force balancing (6, 8, 21, 27, 29, 31, 32), capillary-induced flow (capillary wicking) (9–11, 15, 24, 25, 28, 30), Rayleigh-Taylor wavelength variation (16, 18, 26), and the fragmentation of nonevaporating thin films near the triple contact line (14). All the cited studies found that the mechanism of CHF enhancement depended on the behavior and shape of the liquid-vapor interfaces at spaces between structures that lay under the bubbles.

Therefore, to explain the mechanism of CHF enhancement in general terms, it is necessary to define the behavior and shape of liquid-vapor interfaces at spaces between structures under nucleate bubbles. Because visualization techniques are limited in terms of resolution, these features were previously indirectly explored by evaluating the behavior and shape of spreading (or wicking) surface droplets. Thus, the interfacial behavior at spaces between structures was inferred by the indirect exploration. However, surface wetting characteristics are very sensitive to the environment of the system. Also, the characteristics of a droplet in air on a micro/nano-structured surface are very different from those of a bubble on the same surface (33, 34). Recently, to overcome the limitations of previous visualization techniques, two new techniques have been developed. These are the total reflection technique (35, 36) and the infrared thermometry technique (4, 9, 30, 37–42). However, despite these new experimental endeavors, it remains difficult to visualize the behavior and shape of the liquid-vapor interfaces underneath nucleate bubbles. The reason for this is that the new visualization techniques still have a number

[1]Department of Mechanical Design Engineering, Pukyong National University, 365, Sinseon-ro, Nam-Gu, Busan 48547, Republic of Korea. [2]Department of Mechanical Engineering, Pohang University of Science and Technology, 77, Cheongam-Ro, Nam-Gu, Pohang 37673, Republic of Korea. [3]Division of Advanced Nuclear Engineering, Pohang University of Science and Technology, 77, Cheongam-Ro, Nam-Gu, Pohang 37673, Republic of Korea. [4]Advanced Photon Source, Argonne National Laboratory, 9700 South Cass Avenue, Argonne, IL 60439, USA.
*These authors contributed equally to this work.
†Corresponding author. Email: mhkim@postech.ac.kr

of limitations, such as those imposed by the composition of the structured surface, low spatial resolution (about hundreds of micrometer scales per pixel), etc. Thus, it remains difficult to visualize the behavior and shape of liquid-vapor interfaces at spaces between structures under nucleate bubbles, and the mechanism of CHF enhancement on structured surfaces thus remains unclear.

Here, we introduce synchrotron x-ray imaging with high spatial (~2 μm) and temporal (~20,000 Hz) resolutions as a method to visualize the behavior and shape of liquid-vapor interfaces underneath nucleate bubbles on surfaces with engineered micropillars. In particular, we experimentally show here that wetting characteristics vary with the environment (a nucleate bubble in a pool and a droplet in air on a micropillar surface). On the basis of the visualization data obtained by synchrotron x-ray imaging, we have identified the key CHF enhancement mechanism on the surfaces with micropillars.

## RESULTS
### Pool boiling experiments on surfaces with engineered micropillars

We fabricated micropillar surfaces (using microelectromechanical techniques) on silicon wafers with oxide layers with a thickness of 5000 Å. The test section was composed as follows: one side contained micropillars, which enabled us to quantitatively define the surface wetting characteristics, and the other side contained a thin film heater, which was used to generate the heat required for the nucleate boiling. To obtain the required quantitative geometrical features of the test sections, circular micropillar arrays were fabricated with specific roughness ratios $f$. The roughness ratio is defined as the ratio of the wetted area to the projected area. Figure 1A and Table 1 list the specific geometric features of the micropillar arrays. A thin metal heater, which heated a 10-mm × 10-mm area (total area, 22 mm × 12 mm), was installed on the opposite
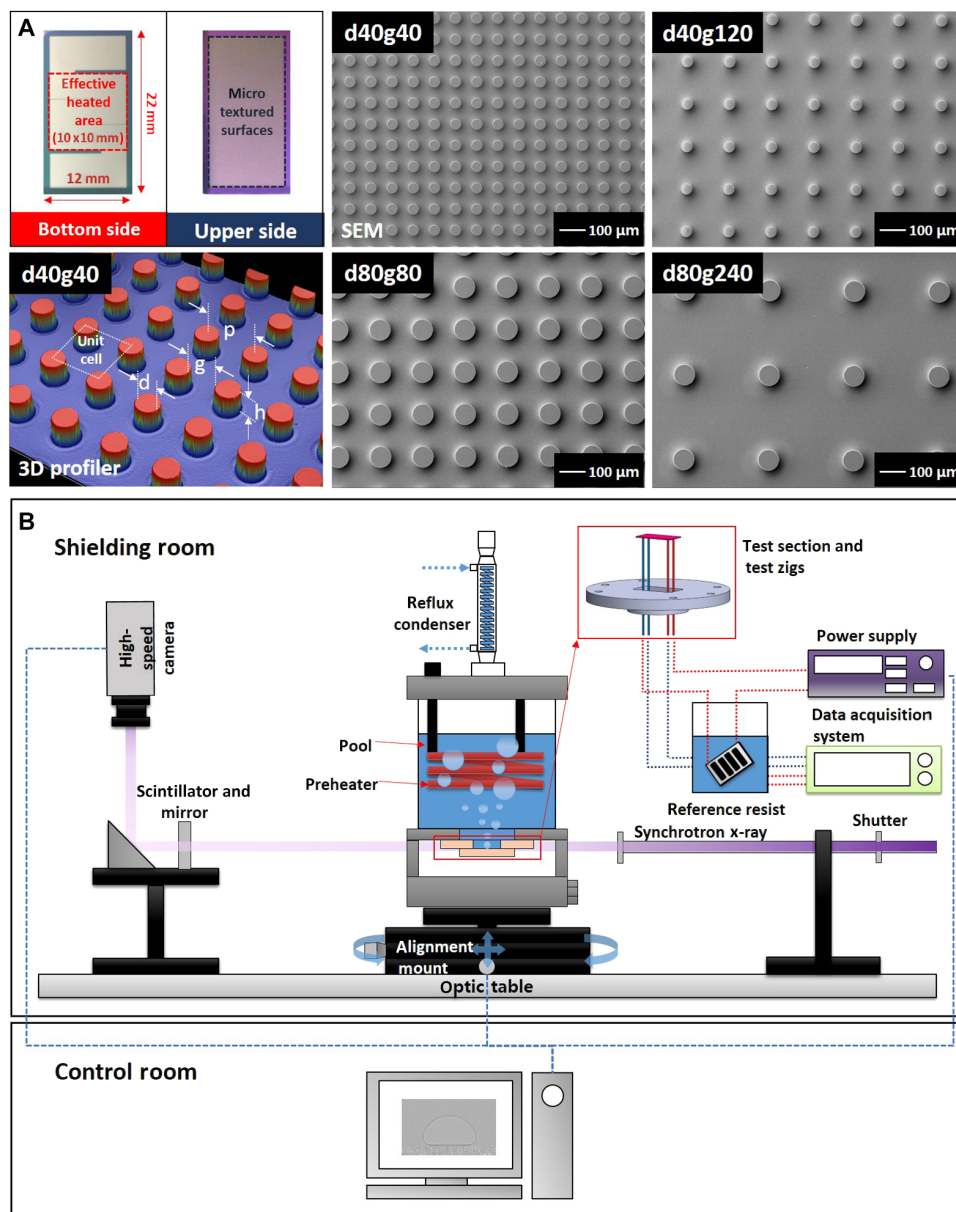


**Fig. 1. Pool boiling experiments.** (**A**) Test sections [field emission scanning electron microscopy (SEM)/3D profiler images]. (**B**) Experimental apparatus.

side of the microstructured surfaces. The specific methods used to prepare the test sections are described in the Supplementary Materials. Figure 1B shows a schematic diagram of the experimental apparatus used in the pool boiling experiment. The test sections were heated electrically using the thin metal heater attached to the other sides of the surfaces.

We used synchrotron x-ray imaging to explore the behavior and shape of liquid-vapor interfaces at spaces between microstructures lying under nucleated bubbles. The experimental platform was located in a room shielded from radioactivity. It is difficult for an experimenter to handle and control the x-ray equipment in the said room. Therefore, all experiments were performed via remote control (from outside the shielding room). We used alignment mounts to align microstructures on the prepared surfaces and to focus the x-rays. The $x$, $y$, and $z$ positions, and the angles of test sections, were thus aligned precisely (within ~1 μm and ~0.001°). Heating of test sections was also remotely controlled. Using the joule heating method, heat flux and wall tempera-

ture data were delivered remotely. The test zig was modified to ensure good penetration by the x-ray beam. X-ray intensity is significantly attenuated by metallic materials, but much less so by polymeric and carbon materials. Therefore, to balance x-ray intensity with the desired insulation and dielectric characteristics, the test zigs were made of polyether ether ketone. Synchrotron x-ray imaging was performed at the Advanced Photon Source (APS) of the Argonne National Laboratory, yielding images of high spatial (~2 μm) and temporal (~20,000 Hz) resolution. Clear images were obtained using a camera with a high frame rate. The x-ray source is described in the Supplementary Materials. In the filtering images, a wet image (no bubble on the surface) is divided with a dry image (a bubble on the surface) based on the Beer-Lambert law. Using the filtering method, the interface is observed.

## Wetting characteristics depending on the environment

Previously, because it was difficult to visualize the behavior and shape of liquid-vapor interfaces under nucleate bubbles, the wetting characteristics of structured surfaces were generally described by the static contact angle or the wicking velocity of a liquid droplet on the surface in air. However, as wetting phenomena are significantly influenced by environmental conditions, it is better to check wetting characteristics in the environment of interest.

The wetting characteristics of micropillar surfaces were measured under ambient conditions (temperature, 23° ± 2°C; relative humidity, 42 ± 3%). A micropipette was used to place 3.0-μl droplets of deionized water on the surfaces. The wetting characteristics of the surfaces, such as the static contact angle and wicking velocity, were measured using an automated goniometer. Each experiment was repeated three times. As shown in Fig. 2 (A and B), no wicking was evident, and the static contact angles on micropillar surfaces were larger than those on an ideal smooth

**Table 1. Specific geometric features of the micropillar arrays.**

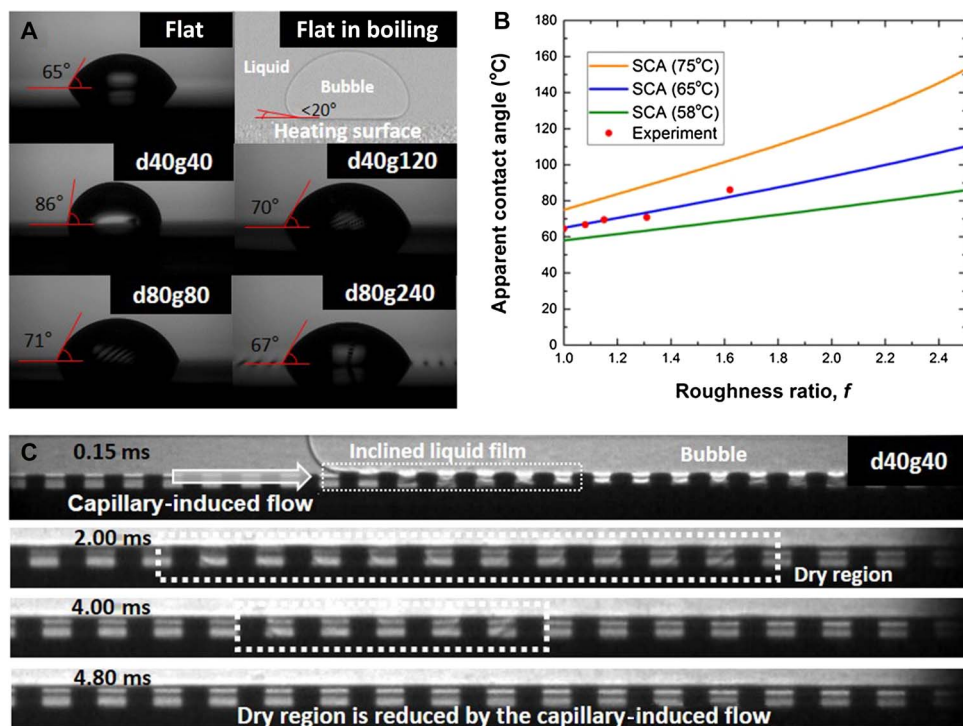| Cases | $d$ (μm) | $g$ (μm) | $p$ (μm) | $h$ (μm) | $f$ |
|---|---|---|---|---|---|
| Flat | — | — | — | — | 1 |
| d40g40 | 40 | 40 | 80 | 20 | 1.62 |
| d40g120 | 40 | 120 | 160 | 20 | 1.15 |
| d80g80 | 80 | 80 | 160 | 20 | 1.31 |
| d80g240 | 80 | 240 | 320 | 20 | 1.08 |



**Fig. 2. Wetting characteristics depending on the environment.** (**A**) Static contact angle (SCA) on the test sections, (**B**) comparison between the measured and estimated SCA on the test sections, and (**C**) wicking phenomena underneath the nucleate bubbles.

surface. In Fig. 2B, measured static contact angles were compared with the estimated angles using the Kang-Jacobi wetting model (43). We found that the static contact angles on the test surfaces were well estimated using the earlier wetting model. In addition, the wetting characteristics of micropillar surfaces were measured under pool boiling conditions (saturation) via synchrotron x-ray imaging. On each surface, the wetting characteristics were visualized at the onset of nucleate boiling and we experimentally confirmed that wicking phenomena were generated, as shown in Fig. 2C.

This comparison of wetting characteristics between ambient and pool boiling conditions showed that the wetting characteristics were significantly influenced by the environment. To understand CHF phenomena, the wetting characteristics of microstructured surfaces should be measured under pool boiling conditions.

## Behavior of the liquid-vapor interfaces underneath nucleate bubbles

We visualized the liquid-vapor interfaces underneath nucleate bubbles at the onset of nucleate boiling ($q'' = 150 \pm 50$ kW/m$^2$, $\Delta T_{sup} = 20° \pm 10°$C). We investigated both flat and micropillar surfaces. When a bubble nucleates on a surface, the dominant forces are the inertia forces caused by the rapid change in density. The change in density occurs during the liquid-to-vapor transition. After nucleation, the bubble grows spherically. However, in the boundary layer near the surface, the outward radial velocity of the fluid is reduced due to friction at the wall. This causes the liquid-vapor interface to be stretched by local differences in the velocity of the fluid. Hence, a liquid film forms underneath the growing bubble (44). As stated previously, the inclined liquid film underneath a bubble initially formed on flat surfaces, as shown in Fig. 3. As the bubbles grew, the contact line at the end of the liquid film propagated more slowly than the liquid-vapor interface. Previous results suggest that nucleate bubbles induce liquid films with multiscale thickness. In particular, they are thought to be composed of three subregions of varying thickness: the absorbed liquid film, the microlayer, and the macrolayer (45). According to the synchrotron x-ray images, the liquid films underneath the nucleate bubbles included films of both micrometer- and macrometer/millimeter-scale thicknesses. Because the thickness of the absorbed liquid film (nanometer-scale thickness) was smaller than the spatial resolution (2 µm) of the synchrotron x-ray beamline, the absorbed liquid film could not be visualized in this study. If we assume that the transition between the micro- and macrolayers occurs at the inflection point of the interface of the liquid film, then the thickness of the microlayer ($\delta = 4$ to $8$ µm) is close to that reported in previous research ($\delta \sim 10$ µm) (40).

The behavior of liquid films on microstructured surfaces was different from the behavior of liquid films on flat surfaces, as shown in Fig. 4. As bubbles started to grow on microstructured surfaces, which had a high roughness ratio ($f = 1.31, 1.62$), an inclined liquid film formed underneath the bubble as shown in Fig. 4 (A and B). The contact lines and interfaces of the liquid film then propagated into the micropillars. Next (after 8 ms, 4.80 ms), the contact lines propagated between the micropillars in the direction parallel to the micropillars. The spaces between the micropillars were filled by the liquid. The thickness of the liquid film was uniform. We compared the liquid-vapor interfaces between the micropillars to the center and side of a nucleate bubble, as shown in Fig. 4A. We found that the liquid-vapor interfaces between the micropillars
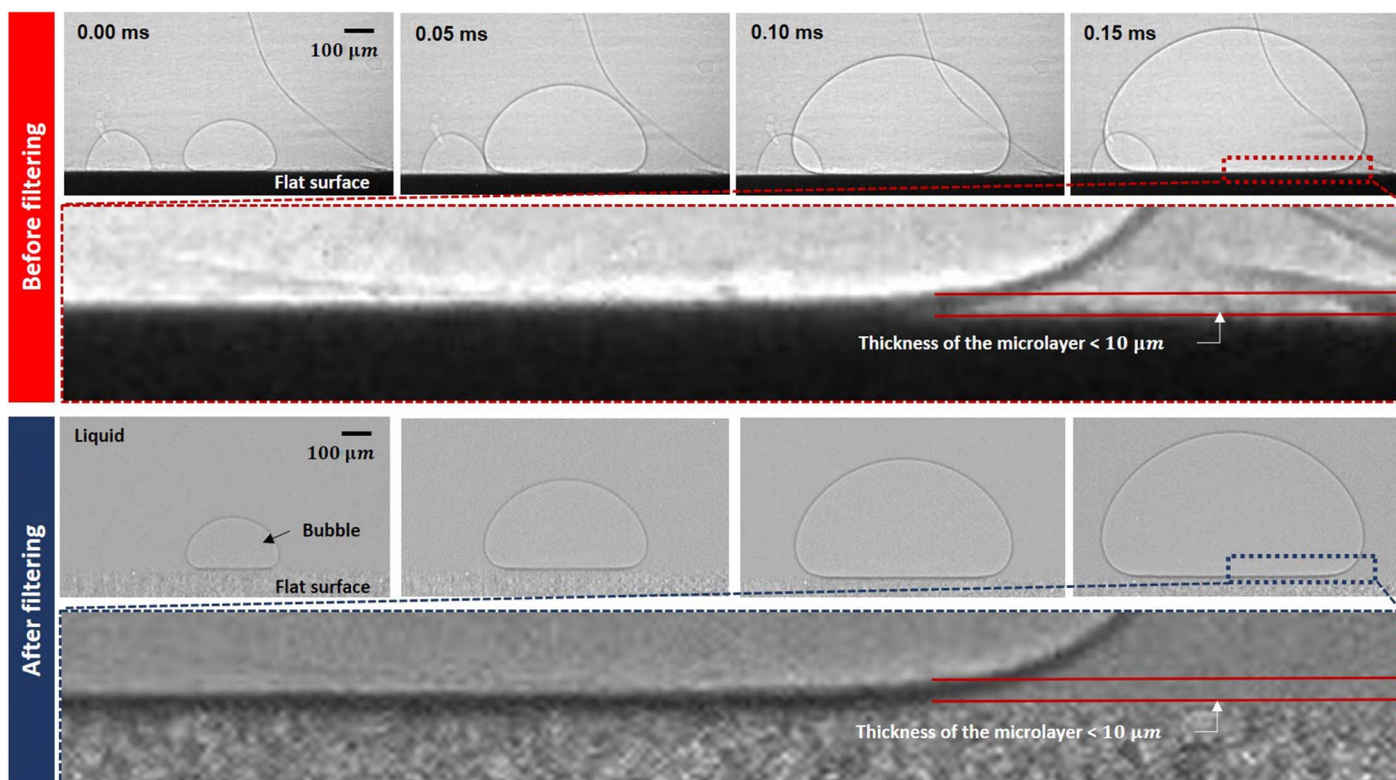


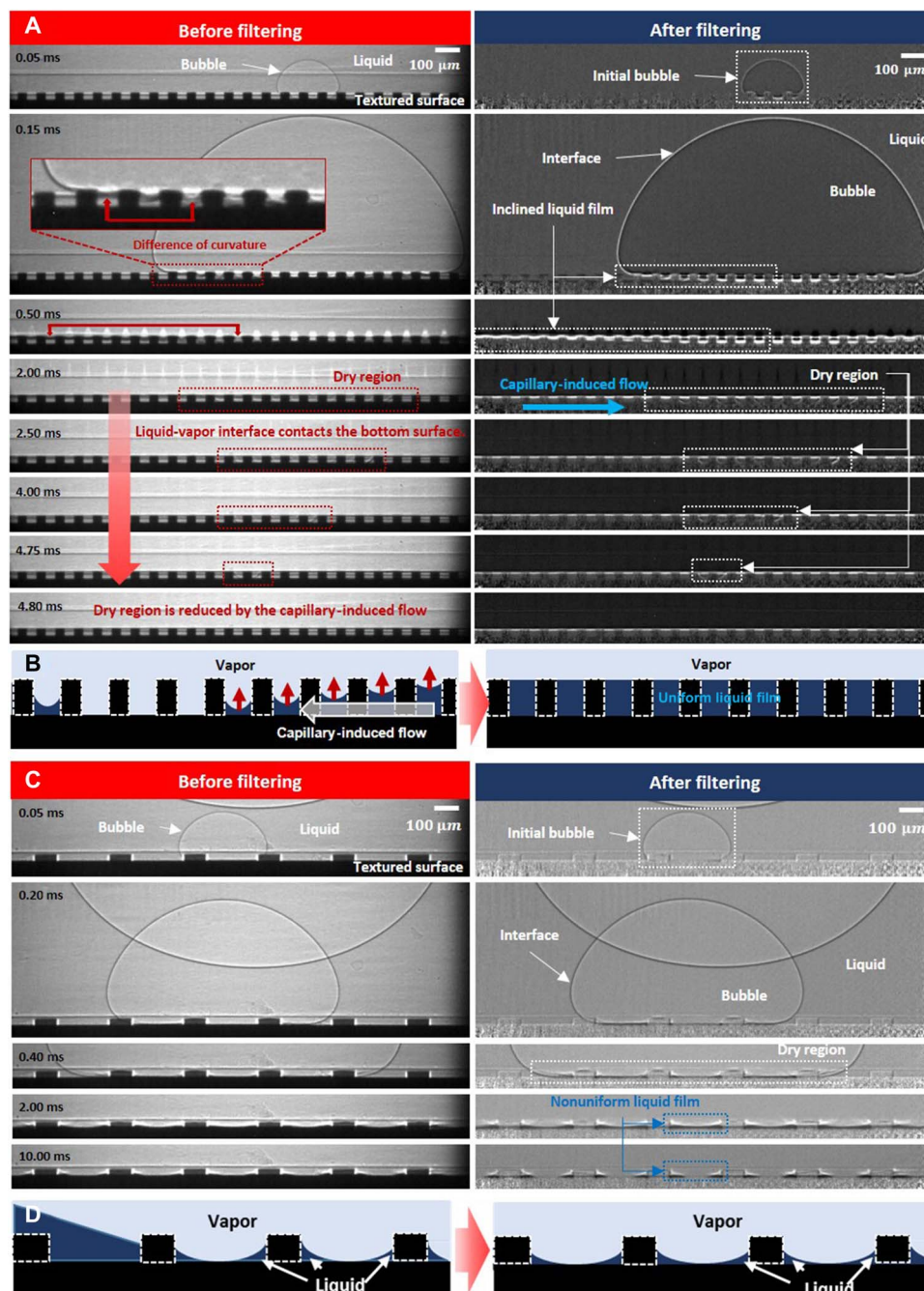**Fig. 3. Visualization of the liquid film underneath a nucleate bubble on a flat surface.**

**Fig. 4. Visualization of the liquid film underneath a nucleate bubble on microtextured surfaces.** (**A**) X-ray images and (**B**) schematic diagram of the high roughness ratio ($f$ = 1.62) surface; (**C**) x-ray images and (**D**) schematic diagram of the low roughness ratio ($f$ = 1.08) surface.

at the center of a nucleate bubble were more concave than those at the side of a nucleate bubble. The capillary pressure was inversely proportional to the radius of curvature of the liquid-vapor interface between the micropillars. Hence, local differences in the capillary pressure between the micropillars at the center and side of a nucleate bubble induced liquid supply through the micropillars from the side to the center of the nucleate bubbles. This liquid supply is known as a capillary-induced flow. It is intensively influenced by the roughness ratio because the capillary pressure between structures is related by the size of the space between structures.

During the propagation of the contact line and liquid-vapor interface of the liquid film on the microstructured surfaces with low roughness ratios ($f$ =1.08, 1.15), parts of the liquid film became caught between the micropillars and remained underneath the growing bubble, as shown in Fig. 4 (C and D). Because the space between the micropillars was larger on the surfaces with low roughness ratios, the capillary force on these surfaces was relatively small. Therefore, to fill all the space between the micropillars, the thickness of the liquid film could not be uniform. The partial volumes of the liquid film did not change significantly with bubble growth. As the bubbles grew, according to our

visualization data, the fragmented liquid volumes were maintained on the surface by very thin liquid layers. These layers linked the volumes and supplied a very small amount of liquid to them. The thickness of the thin layer was expected to be on the order of the spatial resolution of the synchrotron x-ray images (~2 μm). To better understand the liquid flow between the volumes, the behaviors and shapes of the liquid-vapor interfaces underneath the nucleate bubbles on both flat and microstructured surfaces were captured, as shown in movies S1 to S3.

As the heat flux on the surface increased, the number of bubbles generated also increased. These bubbles rose rapidly. On the flat and microstructured surfaces, at the CHF, the dynamics of the contact lines and the liquid-vapor interfaces were extremely vigorous. In one instance, these disappeared from the field of view, as shown in movie S4. Various CHF triggering mechanisms have been proposed. These include blocking of the liquid supply by hydrodynamic instability, the microlayer completely drying out underneath massive bubbles, irreversible development of dry spots, etc. The behavior of the contact lines and liquid-vapor interfaces was visualized in local views (2 mm × 2 mm) of the synchrotron x-ray images. Because we did not fully visualize the motions of the interfaces on the heated surfaces, or observe mushroom bubbles, we could not comprehensively investigate the CHF triggering mechanism in this study. However, the spatial resolution of this visualization technique was sufficiently high to experimentally determine the CHF enhancement mechanism.

On the microstructured surfaces with a high roughness ratio ($f = 1.31$, 1.62), at heat fluxes below the CHF ($f = 1.62$, $q'' = 1554.9 \pm 2.2 \text{ kW/m}^2$, $\Delta T_{sup} = 47.4° \pm 0.82°\text{C}$ and $f = 1.31$, $q'' = 1103.2 \pm 1.3 \text{ kW/m}^2$, $\Delta T_{sup} = 41.5° \pm 0.65°\text{C}$), liquid was supplied through the micropillars. Uniformly thick liquid films formed underneath massive bubbles and remained there. The presence of this phenomenon was confirmed by the oscillating liquid-vapor interfaces between the micropillars, as shown in Fig. 5 and movie S5. As the heat flux on the surfaces increased, the robust, uniformly thick, liquid films underneath the massive bubbles gradually collapsed, and there were frequent contacts between the heated surface and the vapor as the CHF was approached ($f = 1.62$, $q'' = 1856.0 \pm 50 \text{ kW/m}^2$, $\Delta T_{sup} = 52.5° \pm 3.7°\text{C}$ and $f = 1.31$, $q'' = 1443.8 \pm 10 \text{ kW/m}^2$, $\Delta T_{sup} = 50.3° \pm 4.4°\text{C}$). Eventually, at the CHF, the contact lines and liquid-vapor interfaces underneath the massive bubbles will disappear. The frequency of the contact between the heated surfaces and the vapor increased, and the liquid film underneath the massive bubbles collapsed faster on the microstructured surfaces with low roughness ratios ($f = 1.15$, $q'' = 1019.4 \pm 2.4 \text{ kW/m}^2$, $\Delta T_{sup} = 43.5° \pm 1.1°\text{C}$ and $f = 1.08$, $q'' = 1005.7 \pm 6 \text{ kW/m}^2$, $\Delta T_{sup} = 45.6° \pm 3°\text{C}$) than on the surfaces with high roughness ratios, as shown in Fig. 5. This was due to differences in the volumes of liquid transported by the capillary-induced flow on the surfaces with different roughness ratios in equivalent heat flux conditions.

## Relationship between CHF enhancement and the capillary-induced flow

Quantitative analysis of the relationship between CHF enhancement and the capillary-induced flow was carried out by comparing the average liquid supply underneath a growing bubble to CHF enhancement on the test sections. First, we calculated the average liquid supply underneath a growing bubble, $\tilde{V}$. Here, the behavior and shape of liquid-vapor interfaces under nucleate bubbles were visualized from the side via synchrotron x-ray imaging. This view yields two-dimensional (2D) images reflecting the behavior and shape of liquid-vapor interfaces under the

bubbles. When calculating the volume of capillary-driven flow near surface microstructures, we assumed that the liquid-vapor interfaces under nucleate bubbles were equivalent in the circumferential direction. The liquid supply volume of the capillary-induced flow, $\Delta V$, is based on the field of view (2 mm × 2 mm) and the liquid supply time, $\Delta t$. The liquid supply time is the duration of the steady formation of the liquid-vapor interfaces (which we call the filling time). Thus, $\tilde{V}$ is calculated by

$$\tilde{V} = \frac{\Delta V|_{\text{field of view}}}{\Delta t} \tag{1}$$

Initially, on the microstructured surfaces with high roughness ratios ($f = 1.31$, 1.61), an inclined liquid film formed. Subsequently, the spaces between the micropillars were filled by the capillary-induced flow. The thickness of the liquid film was uniform, as shown in Fig. 6A. Therefore, the liquid supply volume caused by the capillary-induced flow is the difference between the volumes of the initially inclined liquid film and the subsequently uniform liquid film

$$\Delta V|_{\text{field of view}} \sim V_0 - V_1 = \frac{\pi D_b^2}{4} h \left[1 - \frac{\pi d^2}{4p^2}\right] - \frac{2}{3} \cdot \frac{\pi D_b^2}{4} h \left[1 - \frac{\pi d^2}{4p^2}\right]$$

$$= \frac{\pi D_b^2}{12} h \left[1 - \frac{\pi d^2}{4p^2}\right] \tag{2}$$

where $D_b$ is the bubble contact diameter, $h$ is the height of the micropillar, $d$ is the diameter of the micropillar, and $p$ is the pitch between the micropillars.

On the microstructured surfaces with low roughness ratios ($f = 1.08$, 1.15), the partial volume of the liquid film remained almost constant as the bubbles grew, as shown in Fig. 6B. Therefore, the liquid volume resulting from the capillary-induced flow can be calculated by summing each partial volume between the micropillars

$$\Delta V|_{\text{field of view}} \sim \#_{\text{unit}} \cdot \Delta V|_{\text{unit}} \sim \#_{\text{unit}} \cdot (V_0 - V_1 - V_2)|_{\text{unit}}$$

$$= \frac{\pi D_b^2}{4p^2} \left[\frac{\pi}{3} \left(\frac{p}{2}\right)^2 \left(h + \frac{d}{g}h\right) - \frac{\pi}{3} \left(\frac{d}{2}\right)^2 \left(\frac{d}{g}h\right) - \pi h \left(\frac{d}{2}\right)^2\right]$$

$$= \frac{\pi D_b^2}{4p^2} \cdot \frac{\pi h}{12g} [p^3 - d^2(p + 2g)] \tag{3}$$

where $\#_{\text{unit}}$ is the unit cell number and $\Delta V_{\text{unit}}$ is the liquid supply volume resulting from the capillary-induced flow on the unit cell bubble, which has contact diameter $D_b$. The height of the micropillar is $h$, $d$ is the diameter of the micropillar, the pitch between the micropillars is $p$, and $g$ is the gap between the micropillars.

The specific liquid supply flow rates, liquid supply volumes, and filling times of each experimental case are described in table S2. The experimental value of the CHF in Fig. 6B was determined by the rapid increase in wall temperature during steady heat flux. When pool boiling experiments are performed using small heated surfaces, the CHF may be influenced by induced liquid flow at the lateral edges. However, in this study, we focused on the CHF enhancement mechanism in play on micropillar surfaces. All test sections, including the flat surface, had equivalent heated areas. CHF enhancement was analyzed in terms of the ratio of
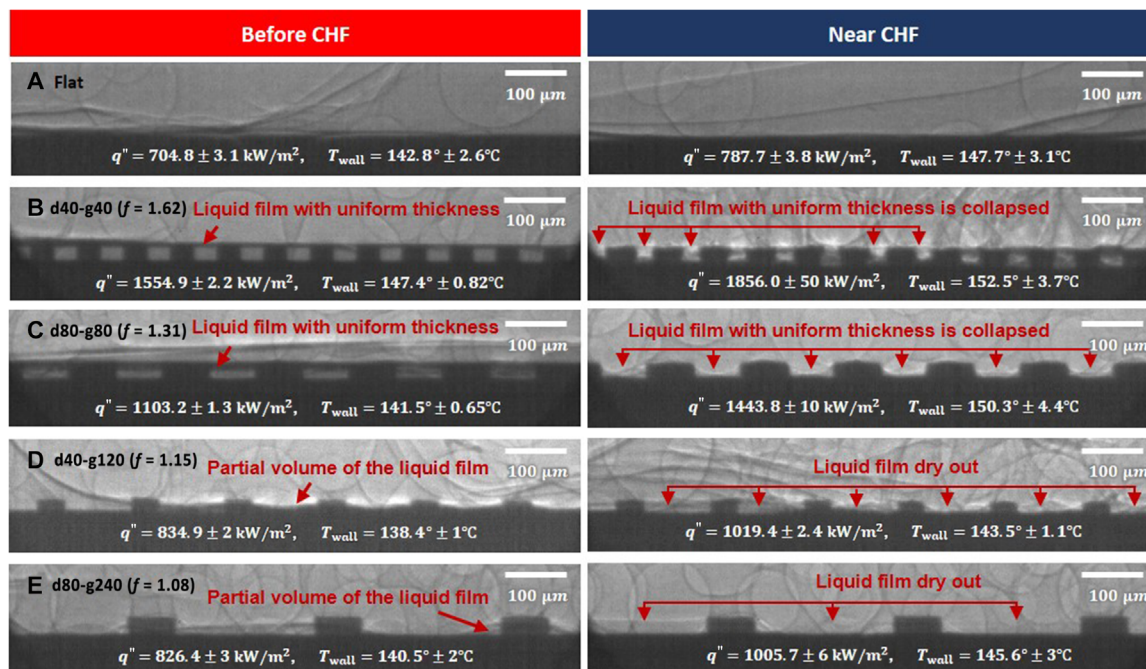
**Fig. 5. Visualization of the liquid film underneath massive bubbles on flat and microtextured surfaces.** (**A**) Flat surface, (**B**) d40-g40 case ($f$ = 1.62), (**C**) d80-g80 case ($f$ = 1.31), (**D**) d40-g120 case ($f$ = 1.15), and (**E**) d80-g240 case ($f$ = 1.08).

the CHFs of test sections to those of a flat surface, as shown in Fig. 6C. Thus, the induced flow of liquid at lateral edges is not the main topic of this study.

We compared the average liquid flow rate underneath a nucleate bubble and the CHF enhancement ratio in the test sections to the roughness ratio. In each case, the trends were similar, monotonically increasing as the roughness ratio increased, as shown in Fig. 6C. On the basis of comparison between the average liquid flow rate underneath a nucleate bubble and CHF enhancement in the test sections, we have experimentally confirmed that capillary-induced flow is the dominant CHF enhancement mechanism on microstructured surfaces. The properties of capillary-induced flow depend on the morphology of the surface on which it takes place.

In recently reported research (9, 10, 30) on silicon oxide surfaces, CHF enhancement was maximized when the spacing between the micropillars was less than 10 μm. These reports found that as the roughness ratios of test sections increased, the capillary forces required to generate the wicking phenomenon also increased, and the viscous forces inhibiting the phenomenon additionally increased. The balance between these forces caused CHF enhancement to be maximized at a specific roughness ratio. Unfortunately, in this study, the average liquid flow rate underneath a nucleate bubble was only measured with relatively large spaces between the micropillars (>40 μm) because of the limited spatial resolution of synchrotron x-ray imaging (2 μm per pixel). When the experimental range of this study is taken into account, our experimental results are similar to previous results. Rather, in the present study, we compared the propagation speeds of the front contact line underneath a growing bubble on microstructured surfaces with micropillar spacings of 40 μm (d40g40, $f$ = 1.62) and 4 μm (d4g4, $f$ = 7.17) to briefly evaluate the specific roughness at the peak of CHF enhancement. In this test, the propagation speed on the surface with the 4-μm (2.96 m/s) micropillar spacing was slower than that of the surface with the 40-μm (4.42 m/s) micropillar spacing. CHF

enhancement (2.23) on the surfaces with large gaps between structures (40 μm) is larger than that (1.60) on the surfaces with small gaps between structures (4 μm). Thus, we experimentally confirmed that the roughness ratios of our test sections were less than the roughness ratio maximizing CHF enhancement.

## DISCUSSION
### Insights into pool boiling CHF enhancement afforded by this study
We obtained the following insights into pool boiling CHF enhancement on micropillar surfaces:

(1) Synchrotron x-ray imaging experimentally confirmed that CHF enhancement on surfaces with engineered micropillars is caused by capillary-induced flow, confirming previous findings.

(2) The wetting characteristics of a droplet in air on the surface differed markedly from those of a bubble in a pool on the same surface. Wetting characteristics were greatly affected by the environment.

(3) Therefore, estimation of CHF enhancement on microstructured surfaces requires capillary-induced flow to be estimated under pool boiling conditions.

(4) In addition, as capillary-induced flow is governed by surface wetting conditions, such as the intrinsic contact angle and roughness ratio, it is necessary to further explore the relationship between capillary-induced flow and surface wetting conditions in a pool boiling system via synchrotron x-ray imaging.

### Possible research by synchrotron x-ray imaging
Synchrotron x-ray imaging allows visualization of the behavior and shape of liquid-vapor interfaces in microspaces, affording high-level resolution in both space and time, no obvious distortion at the liquid-vapor interface, and high transmittance through various materials
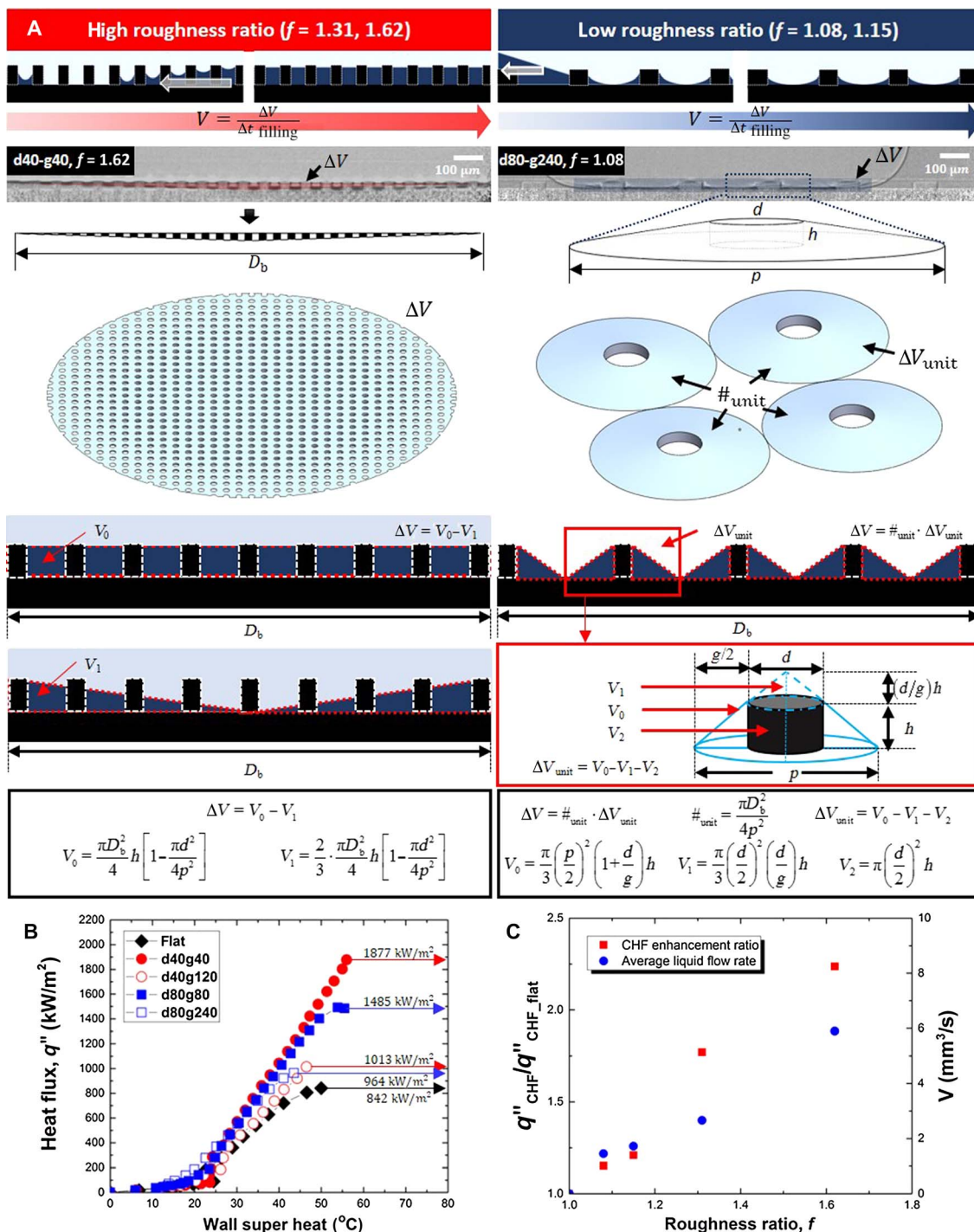
**Fig. 6. Comparison of the average liquid supply underneath a nucleate bubble and CHF enhancement on the test sections.** (**A**) Specific process for calculating the average liquid flow rate underneath a nucleate bubble, (**B**) pool boiling curve, and (**C**) comparison between the CHF enhancement ratio and average liquid flow rate.

(nonmetallic polymers and carbon). Therefore, in pool boiling research, this technique is useful to study the microlayers and wavelengths (measures of instability) under nucleate bubbles. Furthermore, the approach may have applications in various research fields featuring interfacial phenomena, such as boiling, evaporation, condensation, two-phase flow, and surface wettability.

## MATERIALS AND METHODS
### Pool boiling experimental procedure
Before the main experiments, we boiled and degassed the pool of deionized water using a preheater for 2 hours, as shown in Fig. 1B. The pool boiling experiments were conducted at the saturation temperature under atmospheric pressure conditions. The water level and saturation

were maintained using a reflux condenser and a preheater. The test sections were fixed to the test zigs. The test zig was composed of poly-etheretherketone, because this material has the required thermal resistance and x-ray penetration ratio. The test sections were heated electrically by thin metal heaters attached to the opposite sides of the surfaces. The electrical power was supplied by a power supply. An electrical joule heating method was used to measure the heat flux and wall temperature. A data acquisition system was used to measure the voltage and resistance of the test section and the voltage over the reference resistance. We then calculated the heat flux based on the electrical properties and heated area of the test sections. The wall temperature was obtained from the calibration data. The wall temperature depends on the relationship between the temperature and the resistance of the thin metal heater located at the back of the test sections.

## SUPPLEMENTARY MATERIALS

Supplementary material for this article is available at http://advances.sciencemag.org/cgi/content/full/4/2/e1701571/DC1

section S1. Specific processes for the preparation of the test sections
section S2. Synchrotron x-ray images
section S3. Movies with x-ray images
movie S1. Single bubble growing on flat surfaces.
movie S2. Single bubble growing on a high roughness ratio surface.
movie S3. Single bubble growing on a low roughness ratio surface.
movie S4. Behavior of liquid-vapor interfaces on a flat surface (near CHF).
movie S5. Behavior of liquid-vapor interfaces on a high roughness ratio surface (near CHF).
fig. S1. The method used to fabricate the test sections.
table. S1. Detailed information on the x-ray source.
table. S2. Calculated average liquid flow rate underneath a nucleate bubble.
Reference (46)

## REFERENCES AND NOTES

1. S. S. Kutateladze, On the transition to film boiling under natural convection. *Kotloturbostroenie* **3**, 152–158 (1948).
2. N. Zuber, "Hydrodynamic aspects of boiling heat transfer," thesis, UCLA (1959).
3. Y. Haramura, Y. Katto, A new hydrodynamic model of critical heat flux, applicable widely to both pool and forced convection boiling on submerged bodies in saturated liquids. *Int. J. Heat Mass Transf.* **26**, 389–399 (1983).
4. T. G. Theofanous, T. N. Dinh, J. P. Tu, A. T. Dinh, The boiling crisis phenomenon: Part II: Dryout dynamics and burnout. *Exp. Therm. Fluid Sci.* **26**, 793–810 (2002).
5. C. Unal, V. Daw, R. A. Nelson, Unifying the controlling mechanisms for the critical heat flux and quenching: The ability of boiling mechanisms. *Int. J. Heat Mass Transf.* **15**, 25–34 (1992).
6. S. G. Kandlikar, A theoretical model to predict pool boiling CHF incorporating effects of contact angle and orientation. *J. Heat Transfer* **123**, 1071–1079 (2001).
7. B. Bon, J. F. Klausner, E. Mckenna, The hoodoo: A new surface structure for enhanced boiling heat transfer. *J. Thermal Sci. Eng. Appl.* **5**, 011003 (2013).
8. K.-H. Chu, R. Enright, E. N. Wang, Structured surfaces for enhanced pool boiling heat transfer. *Appl. Phys. Lett.* **100**, 241603 (2012).
9. S. H. Kim, G. C. Lee, K. Moriyama, M. H. Kim, H. S. Park, Boiling heat transfer and critical heat flux evaluation of the pool boiling on micro structured surface. *Int. J. Heat Mass Transf.* **91**, 1140–1147 (2015).
10. D. E. Kim, D. I. Yu, S. C. Park, H. J. Kwak, H. S. Ahn, Critical heat flux triggering mechanism on micro-structured surfaces: Coalesced bubble departure frequency and liquid furnishing capability. *Int. J. Heat Mass Transf.* **91**, 1237–1247 (2015).
11. D. E. Kim, S. C. Park, D. I. Yu, M. H. Kim, H. S. Ahn, Enhanced critical heat flux by capillary driven liquid flow on the well-designed surface. *Appl. Phys. Lett.* **107**, 023903 (2015).
12. H. Jo, D. I. Yu, H. Noh, H. S. Park, M. H. Kim, Boiling on spatially controlled heterogeneous surfaces: Wettability patterns on microstructures. *Appl. Phys. Lett.* **106**, 181602 (2015).
13. H. O'Hanley, C. Coyle, J. Buongiorno, T. McKrell, L.-W. Hu, M. Rubner, R. Cohen, Separate effects of surface roughness, wettability and porosity on the boiling critical heat flux. *Appl. Phys. Lett.* **103**, 024102 (2013).
14. A. Zou, S. C. Maroo, Critical height of micro/nano structures for pool boiling heat transfer enhancement. *Appl. Phys. Lett.* **103**, 221602 (2013).
15. H. D. Kim, M. H. Kim, Effect of nanoparticle deposition on capillary wicking that influences the critical heat flux in nanofluids. *Appl. Phys. Lett.* **91**, 014104 (2007).
16. R. Chen, M.-C. Lu, V. Srinivasan, Z. Wang, H. H. Cho, A. Majumdar, Nanowires for enhanced boiling heat transfer. *Nano Lett.* **9**, 548–553 (2009).
17. C. Li, Z. Wang, P.-I. Wang, Y. Peles, N. Koratkar, G. P. Peterson, Nanostructured copper interfaces for enhanced boiling. *Small* **4**, 1084–1088 (2008).
18. M.-C. Lu, R. Chen, V. Srinivasan, V. P. Carey, A. Majumdar, Critical heat flux of pool boiling on Si nanowire array-coated surfaces. *Int. J. Heat Mass Transf.* **54**, 5359–5367 (2011).
19. M. M. Rahman, E. Ölçeroğlu, M. McCarthy, Role of wickability on the critical heat flux of structured superhydrophilic surfaces. *Langmuir* **30**, 11225–11234 (2014).
20. V. Sathyamurthi, H.-S. Ahn, D. Banerjee, S. C. Lau, Subcooled pool boiling experiments on horizontal heaters coated with carbon nanotubes. *J. Heat Transfer* **131**, 071501 (2009).
21. Z. Yao, Y.-W. Lu, S. G. Kandlikar, Effects of nanowire height on pool boiling performance of water on silicon ships. *Int. J. Therm. Sci.* **50**, 2084–2090 (2011).
22. A. R. Betz, J. Jenkins, C.-J. Kim, D. Attinger, Boiling heat transfer on superhydrophilic, superhydrophobic, and superbiphilic surfaces. *Int. J. Heat Mass Transf.* **57**, 733–741 (2013).
23. A. R. Betz, J. Xu, H. Qiu, D. Attinger, Do surfaces with mixed hydrophilic and hydrophobic areas enhance pool boiling? *Appl. Phys. Lett.* **97**, 141909 (2010).
24. H. S. Ahn, G. Park, J. M. Kim, J. Kim, M. H. Kim, The effect of water absorption on critical heat flux enhancement during pool boiling. *Exp. Therm. Fluid Sci.* **42**, 187–195 (2012).
25. B. S. Kim, H. Lee, S. Shin, G. Choi, H. H. Cho, Interfacial wicking dynamics and its impact on critical heat flux of boiling heat transfer. *Appl. Phys. Lett.* **105**, 191601 (2014).
26. S. D. Park, I. C. Bang, Experimental study of a universal CHF enhancement mechanism in nanofluids using hydrodynamic instability. *Int. J. Heat Mass Transf.* **70**, 844–850 (2014).
27. K.-H. Chu, Y. S. Joung, R. Enright, C. R. Buie, E. N. Wang, Hierarchically structured surfaces for boiling critical heat flux enhancement. *Appl. Phys. Lett.* **102**, 151602 (2013).
28. S. Kim, H. D. Kim, H. Kim, H. S. Ahn, H. Jo, J. Kim, M. H. Kim, Effects of nano-fluid and surfaces with nano structure on the increase of CHF. *Exp. Therm. Fluid Sci.* **34**, 487–495 (2010).
29. Z. Yao, Y.-W. Lu, S. G. Kandlikar, Pool boiling heat transfer enhancement through nanostructures on silicon microchannels. *J. Nanotechnol. Eng. Med.* **3**, 031002 (2013).
30. N. S. Dhillon, J. Buongiorno, K. K. Varanasi, Critical heat flux maxima during boiling crisis on textured surfaces. *Nat. Commun.* **6**, 8247 (2015).
31. V. S. Nikolayev, D. A. Beysens, Boiling crisis and non-equilibrium drying transition. *Europhys. Lett.* **47**, 345–351 (1999).
32. V. S. Nikolayev, D. Chatain, Y. Garrabos, D. Beysens, Experimental evidence of the vapor recoil mechanism in the boiling crisis. *Phys. Rev. Lett.* **97**, 184503 (2006).
33. V. Mortazavi, R. M. D'Souza, M. Nosonovsky, Study of contact angle hysteresis using the Cellular Potts Model. *Phys. Chem. Chem. Phys.* **15**, 2749–2756 (2013).
34. S. Yamamoto, K. Andersson, H. Bluhm, G. Ketteler, D. E. Starr, T. Schiros, H. Ogasawara, L. G. M. Pettersson, M. Salmeron, A. Nilsson, Hydroxyl-induced wetting of metals by water at near-ambient conditions. *J. Phys. Chem. C* **111**, 7848–7850 (2007).
35. I.-C. Chu, H. C. No, C.-H. Song, D. J. Euh, Observation of critical heat flux mechanism in horizontal pool boiling of saturated water. *Nucl. Eng. Des.* **279**, 189–199 (2014).
36. I.-C. Chu, H. C. No, C.-H. Song, Visualization of boiling structure and critical heat flux phenomenon for a narrow heating surface in a horizontal pool of saturated water. *Int. J. Heat Mass Transf.* **62**, 142–152 (2013).
37. H. Kim, J. Buongiorno, Detection of liquid–vapor–solid triple contact line in two-phase heat transfer phenomena using high-speed infrared thermometry. *Int. J. Multiphas. Flow* **37**, 166–172 (2011).
38. H. Kim, Y. Park, J. Buongiorno, Measurement of wetted area fraction in subcooled pool boiling of water using infrared thermography. *Nucl. Eng. Des.* **264**, 103–110 (2013).
39. J. Jung, S. J. Kim, J. Kim, Observations of critical heat flux process during pool boiling of FC-72. *J. Heat Transfer* **136**, 041501 (2014).
40. S. Jung, H. Kim, An experimental method to simultaneously measure the dynamics and heat transfer associated with a single bubble during nucleate boiling on a horizontal surface. *Int. J. Heat Mass Transf.* **73**, 365–375 (2014).
41. S. Jung, H. Kim, An experimental study on heat transfer mechanisms in the microlayer using integrated total reflection, laser interferometry and infrared thermometry technique. *Heat Transfer Eng.* **36**, 1002–1012 (2015).
42. D. E. Kim, J. Song, H. Kim, Simultaneous observation of dynamics and thermal evolution of irreversible dry spot at critical heat flux in pool boiling. *Int. J. Heat Mass Transf.* **99**, 409–424 (2016).
43. H. C. Kang, A. M. Jacobi, Equilibrium contact angles of liquid droplets on ideal rough solids. *Langmuir* **27**, 14910–14918 (2011).
44. M. G. Cooper, A. J. P. Lloyd, The microlayer in nucleate pool boiling. *Int. J. Heat Mass Transf.* **12**, 895–913 (1969).
45. J. Kim, Review of nucleate pool boiling bubble heat transfer mechanisms. *Int. J. Multiphas. Flow* **35**, 1067–1076 (2009).
46. R. Xiao, R. Enright, E. N. Wang, Prediction and optimization of liquid propagation in micropillar arrays. *Langmuir* **26**, 15070–15075 (2010).

Citation: D. I. Yu, H. J. Kwak, H. Noh, H. S. Park, K. Fezzaa, M. H. Kim, Synchrotron x-ray imaging visualization study of capillary-induced flow and critical heat flux on surfaces with engineered micropillars. *Sci. Adv.* **4**, e1701571 (2018).

## Synchrotron x-ray imaging visualization study of capillary-induced flow and critical heat flux on surfaces with engineered micropillars

Dong In Yu, Ho Jae Kwak, Hyunwoo Noh, Hyun Sun Park, Kamel Fezzaa and Moo Hwan Kim

| | |
|---|---|
| **ARTICLE TOOLS** | http://advances.sciencemag.org/content/4/2/e1701571 |
| **SUPPLEMENTARY MATERIALS** | http://advances.sciencemag.org/content/suppl/2018/02/16/4.2.e1701571.DC1 |
| **REFERENCES** | This article cites 45 articles, 0 of which you can access for free<br>http://advances.sciencemag.org/content/4/2/e1701571#BIBL |
| **PERMISSIONS** | http://www.sciencemag.org/help/reprints-and-permissions |

Use of this article is subject to the Terms of Service